ANNALS OF THE NEW YORK ACADEMY OF SCIENCES

Pitfalls in using fluorescence tagging of nanomaterials: tecto-dendrimers in skin tissue as investigated by Cluster-FLIM

Pierre Volz,[1] Priscila Schilrreff,[2] Robert Brodwolf,[1] Christopher Wolff,[3] Johannes Stellmacher,[1] Jens Balke,[1] Maria J. Morilla,[2] Christian Zoschke,[3] Monika Schäfer-Korting,[3] and Ulrike Alexiev[1]

[1]Institute of Experimental Physics, Freie Universität Berlin, Berlin, Germany. [2]Nanomedicine Research Program (Departamento de Ciencia y Tecnologia), Universidad Nacional de Quilmes, Buenos Aires, Argentina. [3]Institute for Pharmacy (Pharmacology and Toxicology), Freie Universität Berlin, Berlin, Germany

Addresses for correspondence: Professor Dr. Ulrike Alexiev, Institute of Experimental Physics, Freie Universität Berlin, Arnimallee 14, 14195 Berlin, Germany. ulrike.alexiev@fu-berlin.de; Professor Dr. Monika Schäfer-Korting, Institute for Pharmacy (Pharmacology and Toxicology), Freie Universität Berlin, Königin-Luise Str. 2+4, 14195 Berlin, Germany. monika.schaefer-korting@fu-berlin.de

Targeted topical application promises high drug concentrations in the skin and low systemic adverse effects. To locate drugs and drug-delivery systems like nanocarriers, fluorescent dyes are commonly used as drug surrogates or nanocarrier labels in micrographs of tissue sections. Here, we investigate how labeling degree, concentration of fluorophore, and nanocarrier may affect the interpretation of these micrographs. False-negative penetration results due to inter- and intramolecular quenching effects are likely. Using tecto-dendrimers as an example, we present a detailed analysis of pitfalls in the (semi-)quantitative evaluation of skin nanocarrier penetration. Fluorescence lifetime imaging microscopy (FLIM) allows distinguishing the target fluorescence of dye-tagged nanocarriers from skin autofluorescence, providing a highly sensitive tool for clear-cut localization of the nanocarriers. Cluster-FLIM images reveal that FITC-labeled tecto-dendrimers penetrate the stratum corneum of human skin *ex vivo* and reconstructed human skin but do not cross the tight junction barrier.

Keywords: biomacromolecules; drug delivery system; FLIM; time-resolved fluorescence spectroscopy; tight junctions; reconstructed human skin

Introduction

Nanocarriers have been developed for numerous applications in enhanced or targeted drug delivery. In particular, the notoriously low skin penetration of drugs can be significantly enhanced by nanocarriers,[1] which might allow topical treatment and reduction of systemic adverse effects.[2,3] However, stratum corneum (SC) lipids and corneocytes, filled with keratin, as well as tight junction proteins in viable layers of the epidermis, limit the access to the drug target site. If nanocarriers overcome these barriers, their effects on viable cells and their excretion will be of toxicological concern.

In early phases of nanocarrier development, fluorescent dyes serve as surrogates for loaded drugs or are used as labels to track the nanocarriers themselves. Intensity readings with (confocal) fluorescence microscopy are widely used to obtain a first insight into the penetration profiles and the nanocarrier-modulated uptake of loaded drugs or dyes.[4–6] On the basis of these results, novel concepts in nanocarrier-modulated drug delivery will be improved or terminated. Moreover, fluorescence lifetime imaging microscopy (FLIM) is increasingly becoming an important tool in nanomedical research.[7–12] Given that the fluorescence decay is determined by both the fluorophore and its microenvironment,[13–15] FLIM measurements allow a detailed and highly specific insight into nanocarrier–tissue interactions and provide the

potential to distinguish nanocarrier fluorescence from tissue autofluorescence using novel multivariate analysis tools.[7]

Tecto-dendrimers were developed to overcome the limited tolerability of cationic polyamidoamine dendritic nanocarriers and to increase the number of cavities for drug transport.[16] Tecto-dendrimers induce necrosis specifically in melanoma cells, which might be related to the increased uptake into SK-Mel-28 cells compared with HaCaT cells.[17] Loading methotrexate and zoledronic acid into tecto-dendrimers increased the cytotoxicity of these anticancer drugs to melanoma cells and keratinocytes.[18]

The investigation of novel drug delivery systems like tecto-dendrimers requires a human test platform with *in vivo*–like properties. High safety standards in clinical trials cause tremendous efforts in toxicity testing, and, despite comprehensive testing in the animal, many drug candidates fail because of lacking efficacy or unforeseen adverse effects.[19] Human skin *ex vivo* is as limited as animal tests are of scientific and ethical concern. Three-dimensional skin models (e.g., reconstructed human epidermis and reconstructed human skin (RHS)) from primary human cells proved useful for testing skin absorption and local effects of small molecules with validated test guidelines.[20–22] Aiming not only to assess skin absorption but also to understand the molecular mechanisms of skin permeation, RHS features auspicious advantages. RHS is a metabolically active system,[23] considers fibroblast effects on keratinocyte phenotypes,[24] and can be transferred into more complex test systems, including disease models.[25,26]

Using FITC-labeled tecto-dendrimers as an example, we investigated penetration of the nanocarrier into human skin *ex vivo* as well as into RHS. Moreover, we analyzed the pitfalls from nanocarrier labeling and the consequences for the assessment for cutaneous uptake of nanocarriers. This technical guide will improve nonclinical studies on nanocarrier–tissue interactions and might help to unravel the effect of nanocarriers on tight junction proteins.

Materials and methods

Materials
Collagen I was obtained from Biochrom (Berlin, Germany), cell culture inserts (0.4 μm pore size) were from Corning (Corning, NY). The antibody against claudin-1 (1:200, 1C5-D9, cat-no. H00009076-M01) was purchased from Novus Biologicals (Cambridge, UK), and the Alexa 594–labeled secondary antibody was from Dianova (Hamburg, Germany). Fluorescein isothiocyanate (FITC) was obtained from Thermo Fisher Scientific (Waltham, MA). All other chemicals were of the highest purity available.

Tecto-dendrimers
Synthesis and labeling.   G5G2.5 tecto-denrimers (megamer, MG) were synthesized and purified as described in Schilrreff *et al.*[17] FITC (5 mg/mL) was dissolved in acetone and slowly added to G5G2.5 solutions in phosphate-buffered saline (PBS) (pH 7.4) at various (MG/FITC) molar ratios with increasing excess of FITC. Subsequently, this solution was incubated at 4 °C for 24 h in the dark to allow the amino groups of the G5 core to react with the FITC. The FITC-labeled tecto-dendrimers (MG–FITC) were then separated from free FITC by size-exclusion chromatography on a Sephadex-G25 fine column (GE Healthcare, Chicago, IL). Elution of MG–FITC was facilitated by centrifugation (1000 × *g*) of the loaded column for 1-min runs to obtain the individual fractions.

Determination of MG–FITC concentration.   MG and MG–FITC were analyzed by polyacrylamide gel electrophoresis (SDS-PAGE; 15% acrylamide, 0.375 M Tris–HCl (pH 8.9), and 0.1% (w/v) SDS). Sample MGs of unknown concentrations and reference MGs[17] with known concentrations were solubilized in PBS (pH 7.4) and 17% glycerol. Electrophoresis was performed using a running buffer of 25 mM Tris–HCl (pH 8.8) and 1% (w/v) SDS at a constant voltage of 200 V. After electrophoresis, gels were stained with Coomassie Brilliant Blue R-250 (AppliChem, Darmstadt, Germany) in 20% methanol and 10% acetic acid. Images of the destained gels were taken and band intensities quantified using ImageJ (National Institute of Health). The reference bands of the MGs with known particle concentration were used to generate a calibration curve (band intensity versus concentration) by a linear regression.[17] Using that calibration curve, the concentration (in mol/L) of the MG–FITC sample was determined from the respective band intensities.

Determination of FITC concentration and labeling stoichiometry. Molar concentrations of attached FITC molecules were determined by UV–visible (UV–Vis) spectroscopy using the Lambert–Beer law. The absorbance of FITC at 488 nm (PBS, pH 7.4) and the corresponding extinction coefficient of 65,000 $M^{-1}cm^{-1}$ was used. Reference measurements were performed at alkaline pH with a fully deprotonated fluorescein and an extinction coefficient of 78,000 $\pm$ 7000 $M^{-1}cm^{-1}$ (50 mM potassium phosphate buffer at pH 9),[27] and the corresponding maximum absorbance of the pH-sensitive absorption band was determined. The molar labeling ratio of MG–FITC was then determined as the molar ratio FITC/MG.

Methods for characterization of MG–FITC.

Size and ζ-potential. Size and ζ-potential of MG and MG–FITC samples in PBS were determined by dynamic light scattering and phase analysis light scattering, respectively, using a Nanosizer (ZEN 3600, Malvern Instruments, Malvern, UK). MG–FITC shows comparable size to unlabeled MG.[17]

UV–Vis spectroscopy. Absorption spectra of FITC and MG–FITC were measured either in a 3 × 3 mm quartz cuvette with a UV2450 (Shimadzu, Kyoto, Japan) or using a NanoDrop One (Thermo Fisher Scientific) UV–Vis spectrophotometer. The absorbance was recorded between 300 and 600 nm with a spectral resolution of 0.5 nm.

Fluorescence spectroscopy. Fluorescence emission spectra of FITC and MG–FITC were recorded with a Fluoromax-3 (Horiba Jobin Yvon, Kyoto, Japan) using a 3 × 3 mm quartz cuvette. The temperature was set to 20 °C, and all samples were excited at 488 nm. The fluorescence emission was recorded between 500 and 700 nm with a spectral resolution of 1 nm.

Time-resolved fluorescence and fluorescence lifetime imaging microscopy. Time-resolved fluorescence measurements were conducted in a homemade FLIM setup.[28] The setup consists of an inverted Microscope (IX71, Olympus, Shinjuku, Japan), a tunable ps-supercontinuum laser (SuperK Extreme EUV3, NKT Photonics, Blokken, Denmark), a confocal scanning unit (DCS120, B&H, Berlin, Germany), a hybrid PMT detector (HPM-100-40, B&H) and TCPSC electronics (SPC150, B&H). The FLIM images were recorded using a 40× Objective (Olympus) resulting in a total field of view

side length of 450 μm. FITC and MG–FITC fluorescence was excited at 488 nm and Alexa Fluor 594 fluorescence at 561 nm using an acousto-optical tunable filter (SELECT UV-VIS, NKT Photonics) at 19.5 MHz. Fluorescence emission was spectrally selected by a long-pass filter with $\lambda_{em} > 515$ nm (515LP BrightLine HC, Semrock, Rochester, NY) for FITC and MG–FITC, and with $\lambda_{em} > 575$ nm (575LP ET, Chroma, Rockingham, VT) for Alexa Fluor 594. Emitted photons were collected into 1024 time channels with a channel width of 19.97 picoseconds. The instrument response function of the system was less than 100 ps full width at half-maximum. FLIM data were analyzed using self-written routines in C^{2+}. Fluorescence decay traces of the individual pixels were partitioned into classes (i.e., clusters) using a multivariate pattern-recognition method. False-color images were generated by assigning a distinct color to all pixels containing a fluorescence decay curve that belonged to a certain cluster (e.g., autofluorescence versus MG–FITC fluorescence). Solution FLIM measurements of FITC and MG–FITC were performed using Cellview dishes (Greiner Bio-One, Kremsmünster, Austria).

The recorded solution fluorescence decay traces were fitted using a multiexponential model function:

$$I(t) = \sum_i^n \alpha_i\, e^{-t/\tau_i}, \tag{1}$$

with *n* the total number of decay components, α_i the amplitude, and τ_i the fluorescence lifetime of the *i*th component.[29] The analysis of the time-resolved quenching data[30,31] is based on the mean fluorescence lifetime τ_m calculated by

$$\tau_m = \sum_i^n \frac{\alpha_i \tau_i}{\sum_i^n \alpha_i \tau_i}\, \tau_i. \tag{2}$$

Skin penetration

Skin preparation. Human abdominal skin with no visible damages, stretch marks, or scars was obtained from plastic surgeries with permission and informed consent from male donors (age: 40–60, ethical approval EA4/091/10). After surgery, skin was handled according to standardized procedures to avoid surface contamination with subcutaneous lipids.[20] Cryoconserved and thawed human skin was dermatomized to 500 μm and punched for a surface area of 2 cm².

RHS was grown as described previously.[25] Briefly, we used 0.6×10^6 normal human dermal fibroblasts and 3.0×10^6 normal human keratinocytes per construct, and constructs were cultivated for 3 weeks. Primary normal human keratinocytes and fibroblasts (passage 3, pooled from three donors) were from therapeutically indicated circumcisions (ethical approval EA1/081/13) after parents had signed the written informed consent. Cell culture was performed according to standard operating procedures and referred to good cell culture practice.

For skin penetration studies, 30 μL/cm² of test formulation (50 μmol/L FITC-labeled tecto-dendrimers in PBS (pH 7.4) or an equimolar FITC solution in PBS) was applied onto the tissue surface. To determine the concentration of fluorescein and MG–FITC for application, we used a previously published procedure.[32] In brief, cryosections of tissues were exposed to a series of concentrations of MG–FITC, and the fluorescence intensities were measured. We obtained a linear correlation ($R^2 = 0.9784$) between concentration and fluorescence intensity and proved that 5 μmol/L MG–FITC was 10-fold above our detection limit in epifluorescence microscopy. Assuming a maximal penetration of about 10% of MG–FITC after topical application, we decided to use 50 μmol/L MG–FITC for further experiments. Aqueous FITC solution (50 μmol/L) served as control. Human skin *ex vivo* and RHS were incubated at 37 °C, 5% CO_2 for 6 h with the test solutions. Subsequent to removal of excess formulation with PBS, the skin samples and RHS were snap frozen and sectioned into 7-μm slices (Leica CM 1510S, Wetzlar, Germany).

Skin immunostaining. Immunofluorescence staining for claudin-1 detection was performed according to standard protocols. Briefly, tissue sections were fixed using ice-cold acetone and washed with PBS containing 0.1% bovine serum albumin (BSA) and 0.1% Tween 20 (PBS-BSA-Tween). Subsequently, skin sections were incubated with goat serum (5% in PBS–BSA–Tween) to block unspecific antibody binding. Next, the primary anti-claudin-1 antibody was applied to the tissue sections and incubated overnight at 4 °C. To avoid any spectral overlap with the absorbance and emission of FITC and MG–FITC, we selected a secondary antibody labeled with Alexa Fluor 594. After washing, the secondary antibody was incubated for 1 h at room temperature. The slices were finally washed and subjected to FLIM.

Results

Fluorescence intensity–based evaluation of skin penetration

FITC-labeled tecto-dendrimers (MG–FITC) were topically applied to human skin *ex vivo* (Fig. 1A and B) and RHS (Fig. 1E and F). An aqueous FITC solution served as reference (Fig. 1C and D and G and H, respectively). The fluorescence intensity of FITC alone exceeded the fluorescence intensity of MG–FITC in the skin samples. These results indicate some penetration into the upper epidermis but increased FITC uptake, in both human skin *ex vivo* and RHS. Without further characterization of the fluorescence properties of MG–FITC, this would lead to the conclusion that only a marginal amount of MG–FITC is entering the upper skin compared with FITC alone.

How labeling stoichiometry of MG–FITC affects fluorescence properties

A detailed characterization of MG–FITC as a function of labeling stoichiometry and tecto-dendrimer concentration was performed using UV–Vis and steady-state and time-resolved fluorescence spectroscopy. To achieve a high FITC labeling yield, FITC was added in varying molar excess to the tecto-dendrimers, resulting in labeling stoichiometries ranging from 0.3 to ∼40 molecules of FITC per tecto-dendrimer. For the low-labeling samples, a labeling degree of five FITC molecules per tecto-dendrimer and for the high-labeling samples ∼20–40 FITC molecules per tecto-dendrimer was determined. Unexpectedly, a higher level of labeling did not result in higher fluorescence intensity when compared to equal amounts of FITC (Fig. 2A–D), indicating quenching of the fluorescence. The quenching factor was determined by comparison of FITC and MG–FITC fluorescence (Fig. 2C and D). With regard to visibility of an individual tecto-dendrimer and taking the calculated quenching factor of 5 (low labeling, Fig. 2C) into account, this would result on average in one emitting fluorophore per tecto-dendrimer for the low-labeled samples. However, for the highly labeled sample, only every second or third tecto-dendrimer would fluoresce, based on a quenching factor of ∼90
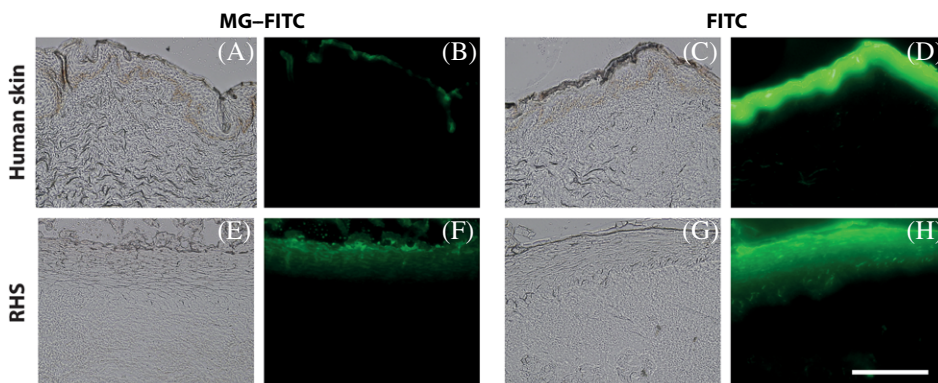
Figure 1. Wide-field microscopy of (A, B, E, F) MG–FITC and (C, F, G, H) FITC topically applied on human skin and RHS. (A, C, E, G) Bright-field images; (B, D, F, H) corresponding epifluorescence images. Scale bar: 200 μm. Conditions as described in Materials and methods.

(high labeling, Fig. 2D) and a labeling degree of 40 FITC/tecto-dendrimer. Thus, a higher labeling, for the case at hand, leads to less visibility of the carrier and consequently to a worse localization in the micrograph. At the same time, the physicochemical properties of the labeled tecto-dendrimer will be changed owing to high labeling with a pH-sensitive (i.e., ionizable) dye. Depending on the environment and pH, the net charge of FITC varies. Consequently, the environment and the labeling degree may affect ζ-potential, electrostatic interactions, and conformation or aggregation of the dendrimer and thus influence skin penetration. The ζ-potential of unlabeled tecto-dendrimers was slightly negative at –4 mV,[17] while after FITC labeling this value became more negative. Furthermore, pH–titration curves of MG–FITC were measured, and the pK_a of bound FITC was determined. The pK_a increases from ~6.5 for free FITC in 10 mM salt to pK_a ~7 for MG–FITC with low labeling and to pK_a ~8 for MG–FITC with high labeling stoichiometry. A shift to higher pK_a values indicates a more negative electrostatic potential,[33,34] consistent with a higher number of negatively charged FITC molecules bound to the tecto-dendrimer.

Factors that could reduce the measured fluorescence intensity are reabsorption (inner filter effect[35]), intra- and intermolecular quenching, and static or dynamic quenching.[31] To address the latter, we determined the fluorescence lifetime of MG–FITC in relation to the lifetime of FITC. In the case of dynamic quenching, the quencher molecule collides with the fluorophore in the excited state

(fluorescence lifetime). Since this is an additional means of depopulating the excited state, it thus affects the rate of fluorescence decay (Fig. 2G and H, red curves). For static quenching, the fluorophore and the quencher form a nonfluorescent complex, with the number of these complexes tending to increase with increasing concentration of quencher molecules. For MG–FITC, the concentration of bound fluorescein increases, and thus the probability to form dark complexes (ground-state quenching) at higher labeling stoichiometries would increase.[36] The nonfluorescent complexes formed in static quenching reduce the observed steady-state fluorescence yield, but have no effect on the fluorescence decay rates for the remaining noncomplexed fluorophores.[31] This would yield different quenching ratios between steady-state and time-resolved fluorescence. Higher ground-state quenching corresponds to a higher quenching factor for steady-state fluorescence. From the comparison of the intensity ratio (Fig. 2E and F) obtained from the steady-state emission curves (Fig. 2C and D) with the fluorescence lifetime ratios (Fig. 2G and H), we conclude that, in the case of the highly labeled sample, a strong ground-state quenching of the attached fluorescein occurs. This only takes place when the molecules are in close proximity (several Å) to each other.[36] Naturally, this probability increases when the labeling stoichiometry is higher and more FITC molecules are attached within one tecto-dendrimer, as explained above. Figure 3A shows the dependence of the quenching factor on the labeling ratio. The data indicate a relative sharp labeling
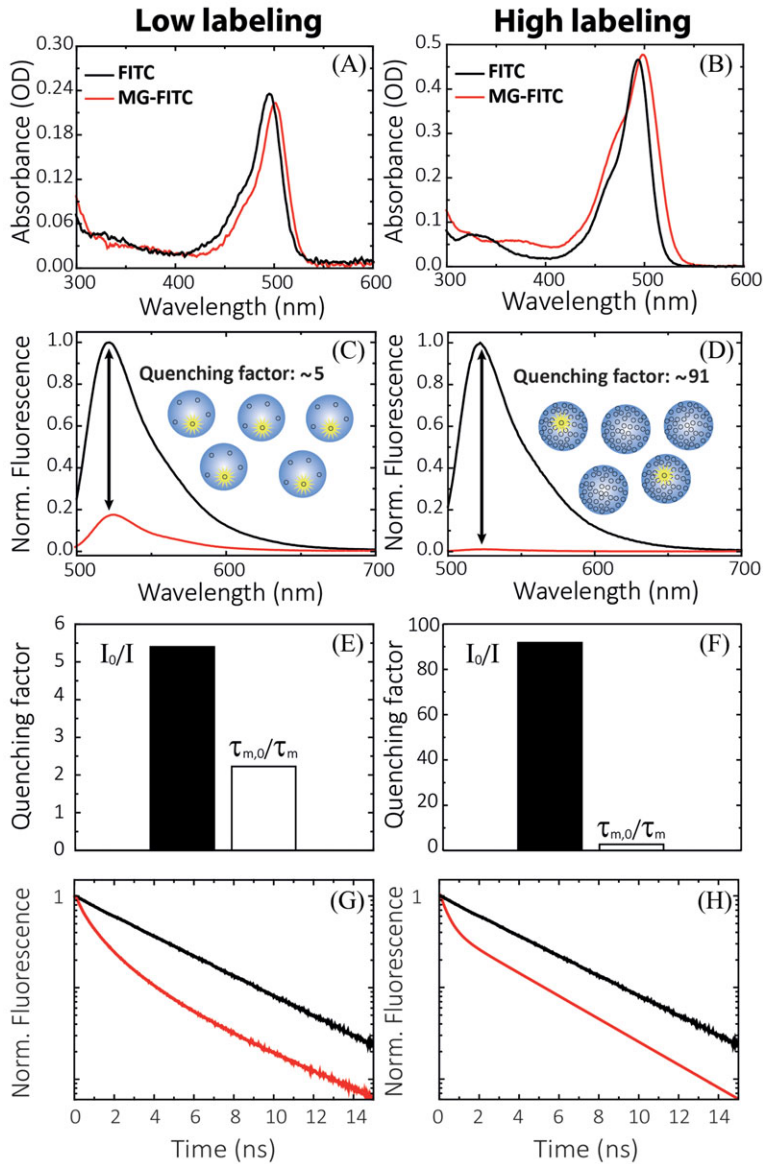
Figure 2. Labeling effects on MG–FITC fluorescence dependent on a high and low labeling ratio. (A, B) Absorbance measurements of FITC (black) and MG–FITC (red) for a low (A) and high (B) labeling ratio (PBS pH 7.4). (C, D) Emission spectra and quenching factor of the FITC (black) and MG–FITC (red) samples shown in A and B. (E, F) Comparison of static and dynamic quenching for high (E) and low (F) labeling ratios, as revealed by steady-state (intensity (I)) and time-resolved fluorescence measurements (mean fluorescence lifetime (τ_m)). The values obtained for FITC (I_0, $\tau_{m,0}$) are compared to those obtained from MG–FITC (I, τ_m). (G, H) Fluorescence decay traces of FITC (black) and MG–FITC (red) at high (G) and low (H) labeling ratios in PBS (pH 7.4). The mean fluorescence lifetimes were determined to be 3.95 ns for FITC and 1.44 ns (high labeling) and 1.75 ns (low labeling) for MG–FITC.

ratio–dependent increase in the quenching factor above a labeling ratio of 7 FITC/tecto-dendrimer.

To test for the dependence on tecto-dendrimer concentration (i.e., the existence of intermolecular quenching), we determined the quenching factor from dilutions of a highly concentrated, highly labeled sample (∼20 FITC/tecto-dendrimer) and used different concentrations of low-labeled samples (<5 FITC/tecto-dendrimer). The results are presented in Figure 3B, where the dilution of
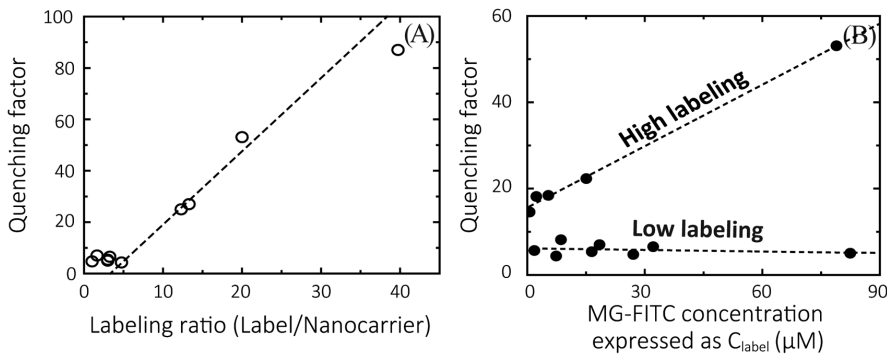
Figure 3. Quenching factors of MG–FITC. (A) Dependence on labeling ratio (FITC/MG). (B) Relationship of MG–FITC concentration and quenching factor. Quenching factors were determined from steady-state fluorescence intensities.

the tecto-dendrimer concentration is expressed via the concentration of the attached FITC molecules. For the low-labeled sample, no changes of the quenching factor as a function of tecto-dendrimer concentration were found. The quenching factor, however, increases for the highly labeled sample with increasing tecto-dendrimer concentration. This leads to the conclusion that, for the highly labeled samples, not only intramolecular but also intermolecular quenching occurs (i.e., the higher the tecto-dendrimer concentration, the fewer fluorescence counts are detected). This behavior renders a quantitative analysis impossible. When extrapolating to a highly diluted sample, the intersection with the *y*-axis in Figure 3B yields a quenching factor of about 18, suggesting that, under highly diluted conditions, one fluorescein per tecto-dendrimer also fluoresces for the highly labeled samples.

Moreover, the complex environment in biological tissue might affect the fluorescence intensities of the label. In skin, the pH profile as well as polarity and viscosity matter, depending on the location of the fluorescently labeled nanocarrier within the lipid layers of the SC or within the more hydrophilic environment in the viable epidermis. Thus, we tested the effect of these parameters on the FITC fluorescence lifetime. Figure 4 shows the fluorescence lifetime curves and quenching analysis for a low-labeled MG–FITC sample as a function of different pH values (Fig. 4A and D), in solutions with different polarity (Fig. 4B and E), and in solutions with different viscosity (Fig. 4C and F). In strong contrast to the effect of low and high labeling on the quenching factor (Fig. 2E–H), the change in the environment only marginally affects the fluores-

cence intensity for the low-labeled sample, as indicated by quenching factors in the range of about 0.5–1.6 when compared with MG–FITC in aqueous solution at pH 7.4.

How background autofluorescence affects evaluation of skin penetration

Intensity-based readings of fluorescence microscopy might be flawed owing to fluorescence properties of the tagged sample and the discrimination of sample fluorescence from background autofluorescence. Figure 5F shows the autofluorescent background of a skin sample. Background-intensity subtraction most likely induces false-positive readings when the threshold intensity is assumed to be low, making a correct assessment of the penetration behavior difficult. In Figure 5H–J, different degrees of background thresholding are presented. Background thresholding was based on the control sample in Figure 5F. To simulate different degrees of background, the threshold was gradually increased to more conservative values in the analysis (Fig. 5H–J). Figure 5G and H show the intensity-based localizations of MG–FITC in the SC and in lower viable epidermal layers. In contrast, a more conservative background thresholding (Fig. 5I and J) limits the localization to the upper SC.

The use of FLIM solves this problem (Fig. 5K–O). Since the fluorescence lifetime depends on the electronic structure of the fluorescing molecule as well as the environment, FLIM allows us to distinguish background fluorescence from target molecule fluorescence via the unique fluorescence lifetime of the target molecule.[10] This procedure, however, becomes more complicated when a complex
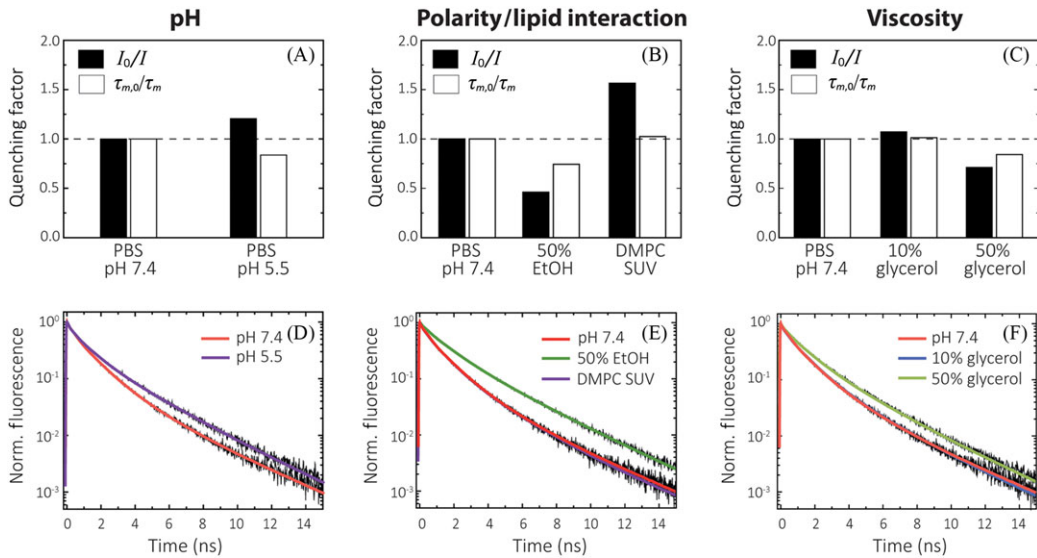
Figure 4. Environmental effects on MG–FITC fluorescence quenching. (A–C): I_0 and $\tau_{m,0}$ were obtained from MG–FITC in PBS at pH 7.4 and compared to MG–FITC fluorescence intensities and mean lifetimes (I, τ_m) in different buffer conditions. (D–F) Environmental effects on the fluorescence decay traces of MG–FITC. The fluorescence decay trace of MG–FITC in PBS (pH 7.4) is shown as reference. (A, D) Comparison of pH 5.5 and 7.4. (B, E) Polarity effect shown for MG–FITC in a 50% PBS/ethanol (EtOH) mixture and in an aqueous solution of small unilamellar vesicles (SUV) containing 0.9 mM DMPC. (C, F) Viscosity effect shown for MG–FITC in PBS/glycerol mixtures with 10% and 50% glycerol.

fluorescence lifetime decay is involved.[37] To meet this challenge, we recently introduced a cluster-based multivariate FLIM analysis tool[7] that allows us to discriminate background from target fluorescence despite complex fluorescence decays and multiple target fluorescence subspecies. Such subspecies may be induced (e.g., by concentration-dependent fluorescence quenching) as observed for the highly labeled MG–FITC. The complex multiexponential decay curves of the autofluorescence background (cyan) and MG–FITC (red) in the skin as extracted by Cluster-FLIM are shown in Figure 5P. Figure 5K–O show the Cluster-FLIM images for both the background autofluorescence (cyan) and the target fluorescence of MG–FITC (red). MG–FITC can be clearly discriminated from autofluorescence, and this is independent of the amount of autofluorescence present in the image. Figure 5Q and R show a higher magnification of the images in Figure 5D and L.

Cluster-FLIM–based evaluation of skin penetration

As determined by Cluster-FLIM, MG-FITC penetrates only into the SC but not into viable epidermal layers. This is the case for both human skin *ex vivo* and RHS (Fig. 6A and D, red and green). Immunofluorescence staining of the tight junction protein claudin-1 in skin[38] was clearly visualized by FLIM. We detected claudin-1 at the keratinocyte membranes up to the stratum granulosum (Fig. 6B and E, yellow), and immunostaining apparently did not influence the detection of MG–FITC, as seen by the comparable results for excised human skin in Figures 5 and 6.

Although we can localize even small amounts of MG–FITC with high precision and resolution by Cluster-FLIM, we did not detect MG–FITC beyond the tight junction protein barrier in the stratum granulosum (dashed white lines). While two different fluorescence decays of MG–FITC in human skin *ex vivo* indicate heterogeneous interactions of MG–FITC with the SC (Fig. 6C, green versus red decay curves), we detected only a single fluorescence lifetime signature of MG–FITC within RHS (Fig. 6F).

Discussion

Nanomedicine describes the successful translation from fundamental nanocarrier research to novel drug-delivery systems. Among more than 50 nanocarrier-based drugs with marketing
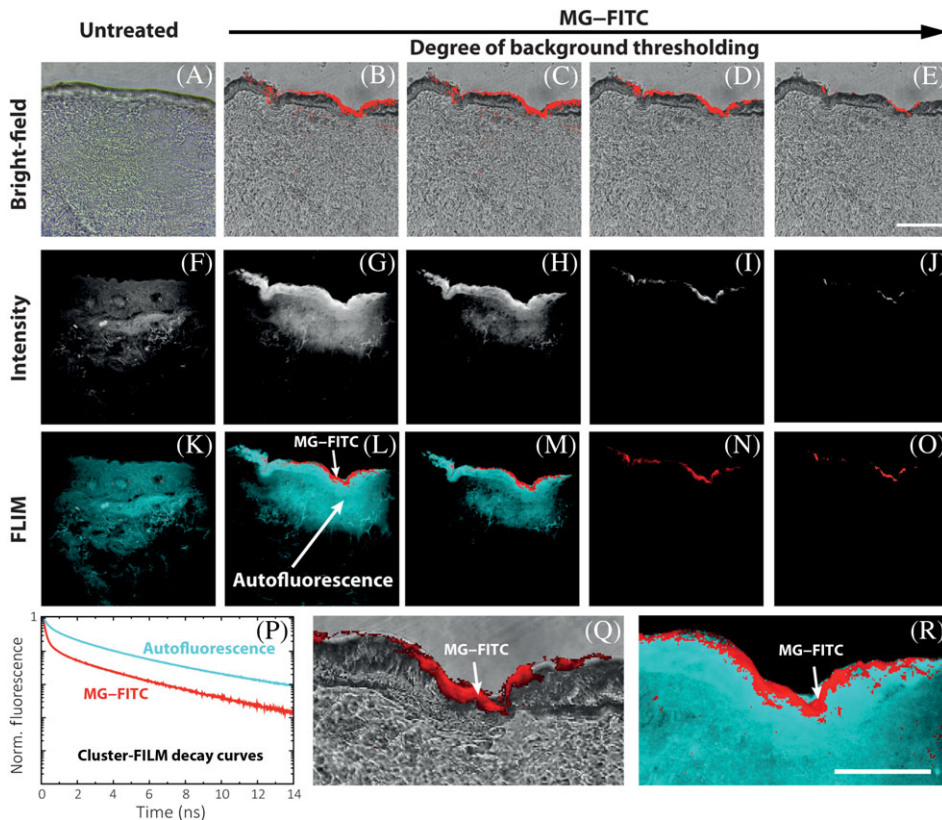
Figure 5. FLIM study of MG–FITC penetration into excised human skin and the effect of background thresholding. (A–E) Bright-field image of untreated (A) and overlay of the bright-field images of MG–FITC-treated (B–E) human skin with the MG–FITC localizations from FLIM analysis as shown in L and M. MG–FITC intensities are false-color coded in red on the basis of fluorescence lifetime cluster analysis. (G–J) Confocal intensities of MG–FITC-treated skin with different background thresholds ((G: 100 cts/px; H: 300 cts/px; I: 1200 cts/px); and J: 2500 cts/px). (F) Confocal intensity of untreated skin. (K–O) False-color–coded FLIM micrographs: autofluorescence is colored in cyan, and MG–FITC fluorescence is colored in red. (P) Normalized fluorescence decay traces (red: MG–FITC; cyan: autofluorescence) as extracted with Cluster-FLIM from A–E and K–O. (Q, R) Magnification of D and L, respectively. Scale bars: 200 μm.

authorization, most are based on two approaches only: liposomal or polyethylene glycol coating. Despite advantages like monodisperse nature, tunable end groups for target recognition, and cleavable spacers for triggered drug release, dendrimeric structures are rarely translated from bench to bedside.[39]

To improve the nonclinical evaluation of novel concepts in drug delivery, we demonstrated the impact of advanced techniques like Cluster-FLIM on the readout of nanocarrier effects. First studies on nanocarriers frequently aim to track them and their cargo to the target site. Fluorescence labeling appears to be as easy and quick, as fluorescence microscopy provides results on nanocarrier uptake. Although guides for standardized fluorescence mea-

surements exist,[40] novel nanocarriers must be characterized in detail for their fluorescence properties after labeling. In most cases, the respective fluorescence label is added in excess to ensure a high labeling yield. Depending on the nanocarrier, this might lead to complications when aiming for an assessment of the penetration profile and a (semi-) quantitative evaluation, as the high labeling degree does not automatically result in higher photon emission and thus higher visibility of the nanocarrier. Additionally, intermolecular quenching effects have to be taken into account, as well as the dependence on environmental factors, such as pH, polarity, or viscosity. In this study, we determined the best labeling stoichiometry to ensure the visibility and linear concentration dependence (Figs. 2 and 3,
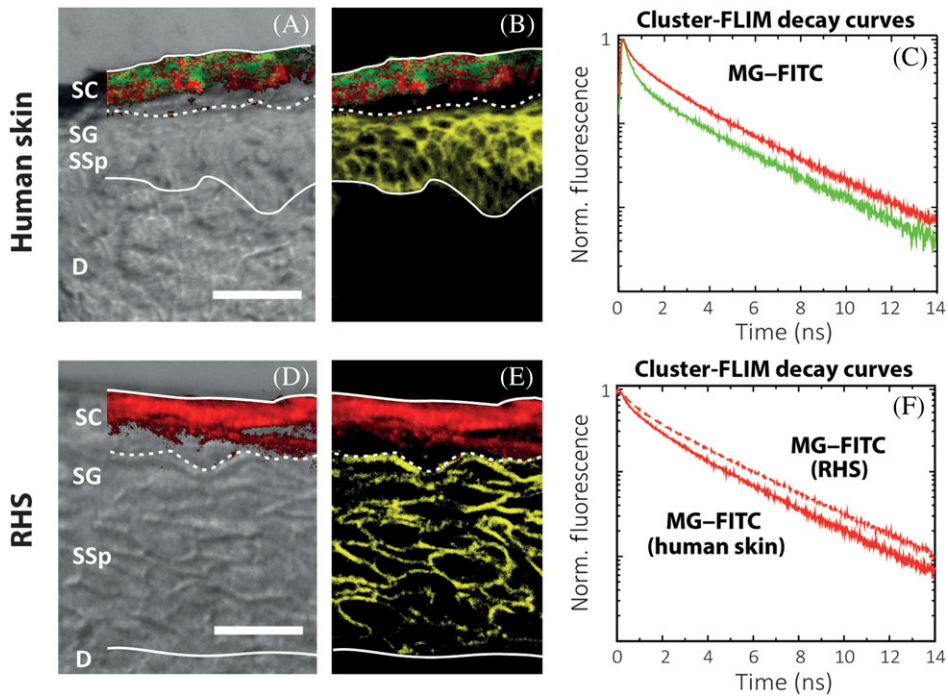
Figure 6. Comparison of MG–FITC penetration and localization of the tight junction protein claudin-1 in human epidermis. (A, D) Overlay image of MG–FITC-treated human skin and RHS. White dashed line indicates the border/barrier of the SC and viable epidermis. (B) False-color–coded FLIM micrograph of the sample shown in A. Claudin-1 is stained in yellow and MG–FITC in green and red. (E) FLIM micrographs of the sample shown in D with claudin-1-staining in yellow and MG–FITC in red. (C) Normalized fluorescence decay traces of MG–FITC as extracted with Cluster-FLIM from B. (F) Comparison of MG–FITC fluorescence decays (red traces) in human skin and RHS (extracted from E). Scale bars: 50 μm; SC, stratum corneum; SG, stratum granulosum; SSp, stratum spinosum; D, dermis.

low-labeled MG–FITC) for quantitative evaluation in skin. In contrast to the high impact of the labeling stoichiometry on fluorescence quenching (Fig. 3), changes in the environment, such as the pH, only marginally affect the fluorescence quenching factor when using the low-labeled MG–FITC sample (Fig. 4A and D). In summary, only a careful analysis of the fluorescence properties of the fluorescently tagged nanocarrier will allow for a quantitative evaluation of the penetration behavior into the skin. Otherwise, the various quenching effects may mask the real localization and concentration of the nanocarrier in skin tissue.

Furthermore, cutaneous autofluorescence limits the sensitivity of intensity-based fluorescence. Since cutaneous autofluorescence depends on the skin color and the body site of the skin,[41] the limit of detection varies from skin sample to skin sample. Moreover, snap freezing or paraffin embedding, standard approaches in the analysis of tissue

samples, induces additional variation. Tissue blocks are cut to slices of a few micrometers, but cutting blocks into slices of exactly the same thickness requires a very well-maintained cryotome and years of experience in cutting. Variation in slice thickness causes variation in autofluorescence within the same study. Taken together, setting the threshold of fluorescence exposure time to exclude autofluorescence remains arbitrary and prone to mistakes. Depending on the bleaching of the fluorescent dye, its intensity will be reduced and false-negative results might occur. If the background autofluorescence is underestimated, as shown in Figure 5G and H, false-positive results will occur. Again using the FITC–tecto-dendrimers as an example, we highlight the importance of correct background subtraction that is not entirely possible using intensity-based fluorescence microscopy. FLIM provides a tool to meet these challenges and to allow distinguishing nanocarrier fluorescence from tissue

autofluorescence, as shown in Figure 5L–O. Although FLIM is a highly specialized microscopic technique and not readily accessible, the number of publications using FLIM as an analytical tool is increasing, indicating the impact of this technique in skin research.[7,9,42–44] FLIM in combination with confocal laser scanning microscopy (CLSM) adds to the advantages of CLSM over conventional fluorescence, imaging the fluorescence lifetime information. Single-photon counting–based FLIM, however, requires longer exposure times than steady-state CLSM, owing to the reduced excitation energies necessary for single-photon counting and the need of a certain number of photons for fluorescence lifetime analyses. New and advanced analysis tools, as shown here with our Cluster-FLIM method, enable accurate fluorescence background subtraction, even at low photon counts.

Employing Cluster-FLIM, tecto-dendrimers were exclusively found within the SC of human skin *ex vivo* and RHS and not within viable layers. This result is consistent with the limited permeation of macromolecules through tight junction proteins.[45] The absence of tecto-dendrimers in viable epidermal layers limits their drug-like use as described for melanoma cells.[17] On the other hand, it reduces the toxicological concern of a topical nanocarrier application, since they access neither viable layers nor the systemic circulation. However, diseases might change the skin barrier function, which could enable tecto-dendrimer penetration into viable layers and require further studies. Among other conditions, nonmelanoma skin cancer alters the expression of tight junction proteins.[46] Finally, a controlled interaction between tight junction proteins and nanocarriers would allow targeted delivery.

To obtain insight into the molecular interactions of tecto-dendrimers with cutaneous lipids and proteins, FLIM analysis provides additional information on the microenvironment of the nanocarrier. Concerning MG–FITC, changes in the pH value or polarity alter the fluorescence lifetime, whereas a slightly increased viscosity does not affect the fluorescence lifetime (fluorescence decay traces in Fig. 4D–F). This might aid further nanocarrier studies on cellular or direct protein interactions to investigate the above-mentioned opening mechanism for tight junctions.

The additional fluorescence lifetime signature in human skin *ex vivo* (Fig. 6C) compared with RHS can be explained by differences in SC lipid composition and/or packing in RHS. Nevertheless, RHS correctly predicted the penetration of tecto-dendrimers into the SC without penetration into the viable epidermis. To the best of our knowledge, this is the first study investigating the cutaneous uptake of tecto-dendrimers into RHS. While the predictive power of reconstructed human epidermis for the absorption of small molecules has been validated,[20] further studies with skin disease models will require RHS with epidermal–dermal interactions. In this study, we proved the utility of RHS for the investigation of tecto-dendrimer penetration.

In conclusion, the Cluster-FLIM–based readout improved the accuracy of nonclinical research during the early development of novel nanocarriers and might provide molecular insights into nanocarrier–tissue interactions. Testing nanocarriers with RHS overcomes the shortage of human skin *ex vivo* and promotes the replacement, reduction, and refinement (3R principle) of animal tests.

Acknowledgments

Competing interests

The authors declare no competing interests.

References

1. Vogt, A., C. Wischke, A.T. Neffe, *et al.* 2016. Nanocarriers for drug delivery into and through the skin—do existing technologies match clinical challenges? *J. Control. Release* **242:** 3–15.

2. Korting, H.C. & M. Schäfer-Korting. 2010. Carriers in the topical treatment of skin disease. *Handb. Exp. Pharmacol.* **2010:** 435–468.

3. Yamamoto, K., A. Klossek, R. Flesch, *et al.* 2016. Core–multishell nanocarriers: transport and release of dexamethasone probed by soft X-ray spectromicroscopy. *J. Control. Release* **242:** 64–70.

4. Alnasif, N., C. Zoschke, E. Fleige, *et al.* 2014. Penetration of normal, damaged and diseased skin—an *in vitro* study on dendritic core–multishell nanotransporters. *J. Control. Release* **185:** 45–50.

5. Campbell, C.S.J., L.R. Contreras-Rojas, M.B. Delgado-Charro, *et al.* 2012. Objective assessment of nanoparticle disposition in mammalian skin after topical exposure. *J. Control. Release* **162:** 201–207.

6. Prow, T.W., N.A. Monteiro-Riviere, A.O. Inman, *et al.* 2012. Quantum dot penetration into viable human skin. *Nanotoxicology* **6:** 173–185.

7. Alexiev, U., P. Volz, A. Boreham, *et al.* 2017. Time-resolved fluorescence microscopy (FLIM) as an analytical tool in skin nanomedicine. *Eur. J. Pharm. Biopharm.* **116:** 111–124.

8. Leite-Silva, V.R., M. Le Lamer, W.Y. Sanchez, *et al.* 2013. The effect of formulation on the penetration of coated and uncoated zinc oxide nanoparticles into the viable epidermis of human skin *in vivo*. *Eur. J. Pharm. Biopharm.* **84:** 297–308.

9. Zhu, Y., C.-S. Choe, S. Ahlberg, *et al.* 2015. Penetration of silver nanoparticles into porcine skin *ex vivo* using fluorescence lifetime imaging microscopy, Raman microscopy, and surface-enhanced Raman scattering microscopy. *J. Biomed. Opt.* **20:** 051006.

10. Boreham, A., T.-Y. Kim, V. Spahn, *et al.* 2011. Exploiting fluorescence lifetime plasticity in FLIM: target molecule localization in cells and tissues. *ACS Med. Chem. Lett.* **2:** 724–728.

11. Huck, V., C. Gorzelanny, K. Thomas, *et al.* 2016. From morphology to biochemical state—intravital multiphoton fluorescence lifetime imaging of inflamed human skin. *Sci. Rep.* **6:** https://doi.org/10.1038/srep22789.

12. Roberts, M.S., Y. Dancik, T.W. Prow, *et al.* 2011. Noninvasive imaging of skin physiology and percutaneous penetration using fluorescence spectral and lifetime imaging with multiphoton and confocal microscopy. *Eur. J. Pharm. Biopharm.* **77:** 469–488.

13. Boreham, A., M. Pfaff, E. Fleige, *et al.* 2014. Nanodynamics of dendritic core–multishell nanocarriers. *Langmuir* **30:** 1686–1695.

14. Boreham, A., J. Pikkemaat, P. Volz, *et al.* 2016. Detecting and quantifying biomolecular interactions of a dendritic polyglycerol sulfate nanoparticle using fluorescence lifetime measurements. *Molecules* **21:** E22.

15. Marcu, L. 2012. Fluorescence lifetime techniques in medical applications. *Ann. Biomed. Eng.* **40:** 304–331.

16. Tomalia, D.A., S. Uppuluri, D.R. Swanson, *et al.* 2000. Dendrimers as reactive modules for the synthesis of new structure-controlled, higher-complexity megamers. *Pure Appl. Chem.* **72:** 2343.

17. Schilrreff, P., C. Mundina-Weilenmann, E.L. Romero, *et al.* 2012. Selective cytotoxicity of PAMAM G5 core–PAMAM G2.5 shell tecto-dendrimers on melanoma cells. *Int. J. Nanomed.* **7:** 4121–4133.

18. Schilrreff, P., G. Cervini, E.L. Romero, *et al.* 2014. Enhanced antimelanoma activity of methotrexate and zoledronic acid within polymeric sandwiches. *Colloids Surf. B Biointerfaces* **122:** 19–29.

19. Arrowsmith, J. 2011. Trial watch: phase II failures: 2008–2010. *Nat. Rev. Drug Discov.* **10:** 328–329.

20. Schäfer-Korting, M., U. Bock, W. Diembeck, *et al.* 2008. The use of reconstructed human epidermis for skin absorption testing: results of the validation study. *Altern. Lab. Anim.* **36:** 161–187.

21. OECD 428. 2004. Test No. 428: skin absorption: *in vitro* method. In *OECD Guidelines for the Testing of Chemicals, Section 4: Health Effects.* OECD Publishing. Accessed August 17, 2017. https://doi.org/10.1787/9789264071087-en.

22. OECD 439. 2015. Test No. 439: *in vitro* skin irritation. In *OECD Guidelines for the Testing of Chemicals, Section 4: Health Effects.* OECD Publishing. Accessed August 17, 2017. https://doi.org/10.1787/9789264242845-en.

23. Bätz, F.M., W. Klipper, H.C. Korting, *et al.* 2013. Esterase activity in excised and reconstructed human skin—biotransformation of prednicarbate and the model dye fluorescein diacetate. *Eur. J. Pharm. Biopharm.* **84:** 374–385.

24. Berroth, A., J. Kuhnl, N. Kurschat, *et al.* 2013. Role of fibroblasts in the pathogenesis of atopic dermatitis. *J. Allergy Clin. Immunol.* **131:** 1547–1554.

25. Zoschke, C., M. Ulrich, M. Sochorová, *et al.* 2016. The barrier function of organotypic non-melanoma skin cancer models. *J. Control. Release* **233:** 10–18.

26. Hönzke, S., C. Gerecke, A. Elpelt, *et al.* 2016. Tailored dendritic core–multishell nanocarriers for efficient dermal drug delivery: a systematic top-down approach from synthesis to preclinical testing. *J. Control. Release* **242:** 50–63.

27. Molecular Probes, Inc. 2015. Certificate of analysis. 2017.

28. Boreham, A., R. Brodwolf, K. Walker, *et al.* 2016. Time-resolved fluorescence spectroscopy and fluorescence lifetime imaging microscopy for characterization of dendritic polymer nanoparticles and applications in nanomedicine. *Molecules* **22:** E17.

29. Kim, T.Y., K. Winkler & U. Alexiev. 2007. Picosecond multidimensional fluorescence spectroscopy: a tool to measure real-time protein dynamics during function. *Photochem. Photobiol.* **83:** 378–384.

30. Volz, P., N. Krause, J. Balke, *et al.* 2016. Light and pH-induced changes in structure and accessibility of transmembrane helix B and its immediate environment in channelrhodopsin-2. *J. Biol. Chem.* **291:** 17382–17393.

31. Alexiev, U. & D.L. Farrens. 2014. Fluorescence spectroscopy of rhodopsins: insights and approaches. *Biochim. Biophys. Acta* **1837:** 694–709.

32. Lombardi Borgia, S., M. Regehly, R. Sivaramakrishnan, *et al.* 2005. Lipid nanoparticles for skin penetration enhancement-correlation to drug localization within the particle matrix as determined by fluorescence and parelectric spectroscopy. *J. Control. Release* **110:** 151–163.

33. Alexiev, U., P. Scherrer, T. Marti, *et al.* 1995. Time-resolved surface charge change on the cytoplasmic side of bacteriorhodopsin. *FEBS Lett.* **373:** 81–84.

34. Möller, M. & U. Alexiev. 2009. Surface charge changes upon formation of the signaling state in visual rhodopsin. *Photochem. Photobiol.* **85:** 501–508.

35. Fonin, A.V., A.I. Sulatskaya, I.M. Kuznetsova, *et al.* 2014. Fluorescence of dyes in solutions with high absorbance. Inner filter effect correction. *PLoS One* **9:** e103878.

36. Runnels, L.W. & S.F. Scarlata. 1995. Theory and application of fluorescence homotransfer to melittin oligomerization. *Biophys. J.* **69:** 1569–1583.

37. Boreham, A., R. Brodwolf, M. Pfaff, *et al.* 2014. Temperature and environment dependent dynamic properties of a dendritic polyglycerol sulfate. *Polym. Adv. Technol.* **25:** 1329–1336.

38. Kirschner, N. & J.M. Brandner. 2012. Barriers and more: functions of tight junction proteins in the skin. *Ann. N.Y. Acad. Sci.* **1257:** 158–166.

39. Caster, J.M., A.N. Patel, T. Zhang, *et al.* 2017. Investigational nanomedicines in 2016: a review of nanotherapeutics currently undergoing clinical trials. *Wiley Interdiscip. Rev. Nanomed. Nanobiotechnol.* **9:** e1416.

40. Resch-Genger, U., K. Hoffmann & A. Hoffmann. 2008. Standardization of fluorescence measurements: criteria for the choice of suitable standards and approaches to fit-for-purpose calibration tools. *Ann. N.Y. Acad. Sci.* **1130:** 35–43.

41. Czekalla, C., K.H. Schönborn, N. Döge, *et al.* 2017. Body regions have an impact on the collagen/elastin index of the skin measured by non-invasive *in vivo* vertical two photon microscopy. *Exp. Dermatol.* **26:** 822–824.

42. Ostrowski, A., D. Nordmeyer, A. Boreham, *et al.* 2014. Skin barrier disruptions in tape stripped and allergic dermatitis models have no effect on dermal penetration and systemic distribution of AHAPS-functionalized silica nanoparticles. *Nanomedicine* **10:** 1571–1581.

43. Witting, M., A. Boreham, R. Brodwolf, *et al.* 2015. Interactions of hyaluronic acid with the skin and implications for the dermal delivery of biomacromolecules. *Mol. Pharm.* **12:** 1391–1401.

44. Liu, D.C., A.P. Raphael, D. Sundh, *et al.* 2012. The human stratum corneum prevents small gold nanoparticle penetration and their potential toxic metabolic consequences. *J. Nanomater.* **2012**. https://doi.org/10.1155/2012/721706.

45. Kirschner, N., R. Rosenthal, M. Furuse, *et al.* 2013. Contribution of tight junction proteins to ion, macromolecule, and water barrier in keratinocytes. *J. Invest. Dermatol.* **133:** 1161–1169.

46. Rachow, S., M. Zorn-Kruppa, U. Ohnemus, *et al.* 2013. Occludin is involved in adhesion, apoptosis, differentiation and Ca^{2+}-homeostasis of human keratinocytes: implications for tumorigenesis. *PLoS One* **8:** e55116.